



AMERICAN METEOROLOGICAL SOCIETY

Bulletin of the American Meteorological Society

EARLY ONLINE RELEASE

This is a preliminary PDF of the author-produced manuscript that has been peer-reviewed and accepted for publication. Since it is being posted so soon after acceptance, it has not yet been copyedited, formatted, or processed by AMS Publications. This preliminary version of the manuscript may be downloaded, distributed, and cited, but please be aware that there will be visual differences and possibly some content differences between this version and the final published version.

The DOI for this manuscript is doi: [10.1175/2011BAMS3039.1](https://doi.org/10.1175/2011BAMS3039.1)

The final published version of this manuscript will replace the preliminary version at the above DOI once it is available.



1 **Globally gridded satellite (GridSat) observations for climate** 2 **studies**

3 Kenneth R. Knapp¹, Steve Ansari¹, Caroline L. Bain², Mark A. Bourassa³, Michael J.
4 Dickinson⁴, Chris Funk⁵, Chip N. Helms⁶, Christopher C. Henon⁷, Christopher D. Holmes⁸,
5 George J. Huffman⁹, James P. Kossin¹, Hai-Tien Lee¹⁰, Alexander Loew¹¹, Gudrun
6 Magnusdottir¹²

¹ NOAA National Climatic Data Center, Asheville, North Carolina

² University of California at Irvine, Irvine, California now at Met Office, Exeter, Devon, UK

³ Florida State University, Tallahassee, Florida

⁴ Department of Earth and Atmospheric Sciences, The University at Albany/SUNY, Albany,
New York, now at WeatherPredict Consulting, Wakefield, Rhode Island

⁵ USGS Center for Earth Resource Observations and Science, Santa Barbara, California

⁶ University of North Carolina Asheville, Asheville, North Carolina, now at Florida State
University, Tallahassee, Florida

⁷ University of North Carolina Asheville, Asheville, North Carolina

⁸ Department of Earth and Planetary Science, Harvard University, Cambridge, Massachusetts

⁹ Science Systems and Applications, Inc. and NASA Goddard Space Flight Center, Greenbelt,
Maryland

¹⁰ Cooperative Institute for Climate and Satellites (CICS), University of Maryland, College Park,
Maryland

¹¹ Max-Planck-Institute for Meteorology, KlimaCampus, Hamburg, Germany

¹² University of California at Irvine, Irvine, California

7 To be submitted to the *Bulletin of the American Meteorological Society*

8 Capsule Summary: “Calibrated and mapped geostationary data provide historical satellite
9 data to non-satellite experts for studies of weather and climate.”

10 Corresponding Author:

11 Kenneth R. Knapp

12 NOAA/National Climatic Data Center

13 151 Patton Ave.

14 Asheville, NC 28801

15 Ken.Knapp@noaa.gov

16 Phone: 828-271-4339

17 Fax: 828-271-4328

18

19 **Abstract**

20 Geostationary satellites have provided routine, high temporal resolution Earth observations
21 since the 1970s. Despite the long period of record, use of these data in climate studies has been
22 limited for numerous reasons, among them: no central archive of geostationary data for all
23 international satellites exists, full temporal and spatial resolution data are voluminous, and
24 diverse calibration and navigation formats encumber the uniform processing needed for multi-
25 satellite climate studies. The International Satellite Cloud Climatology Project set the stage for
26 overcoming these issues by archiving a subset of the full resolution geostationary data at ~10 km
27 resolution at 3 hourly intervals since 1983. Recent efforts at NOAA's National Climatic Data
28 Center to provide convenient access to these data include remapping the data to a standard map
29 projection, recalibrating the data to optimize temporal homogeneity, extending the record of
30 observations back to 1980, and reformatting the data for broad public distribution. The Gridded
31 Satellite (GridSat) dataset includes observations from the visible, infrared window, and infrared
32 water vapor channels. Data are stored in the netCDF format using standards that permit a wide
33 variety of tools and libraries to process the data quickly and easily. A novel data layering
34 approach, together with appropriate satellite and file metadata, allows users to access GridSat
35 data at varying levels of complexity based on their needs. The result is a climate data record
36 already in use by the meteorological community. Examples include reanalysis of tropical
37 cyclones, studies of global precipitation, and detection and tracking of the intertropical
38 convergence zone.

39

40 With the recent passing of the 50th anniversary of the first U.S. weather satellite,
41 questions on how to best use historical satellite data come to the forefront of the discussion on
42 climate observation. There are now over 30 years of globally sampled geostationary and polar
43 satellite data, and while the visible and infrared imaging instruments on the satellites were not
44 specifically designed for climate purposes, the record has great potential to be used for
45 observational climate studies. With this in mind, NOAA recently embarked on an effort to derive
46 Climate Data Records (CDRs) from environmental satellite data (National Research Council
47 2004), including geostationary satellites. At present, most CDRs derived from historical satellites
48 are based on polar orbiting instruments, such as sea surface temperature data (Reynolds et al.
49 2002). Climatic use of geostationary data has been limited largely to teams of satellite experts –
50 e.g., the international community activities of the Global Energy and Water Experiment
51 (GEWEX) such as the International Satellite Cloud Climatology Project (ISCCP) and the Global
52 Precipitation Climatology Project (GPCP).

53 Numerous issues hinder use of the complete global geostationary data record by the
54 climate research community. First, each country archives its own geostationary data. Thus, to
55 obtain global data, one could access data from the U.S. (for the Geostationary Operational
56 Environmental Satellites, GOES), Europe (for the Meteorological Satellites, Meteosat), Japan
57 (for the Geostationary Meteorological Satellites, GMS, and Multi-functional Transport Satellite,
58 MTSAT) and China (for the Feng Yun, FY, geostationary satellite). Additionally, users might
59 access geostationary data from other nations for climate studies, such as India, South Korea and
60 Russia. Second, the volume of full resolution data can be unwieldy for any study at climate time-
61 scales. Third, the data format from each agency will be heterogeneous; furthermore, the data
62 from any one agency may have multiple file formats. Assuming a user can overcome these

63 hurdles, they must also calibrate (i.e., calculate radiances and brightness temperatures from the
64 data) and navigate (i.e., determine the latitude and longitude for each image pixel) the data from
65 each satellite.

66 As mentioned, the ISCCP and GPCP projects are two of the few climate uses of
67 geostationary data prior to 2000. This is due in part to the international collaboration that
68 overcame the hindrances described above. In doing so, the ISCCP stored a subset of satellite data
69 at NCDC called ISCCP B1 that included data from each international meteorological satellite.
70 However, necessary information about the data such as file format, navigation algorithms, etc.
71 were not archived. This caused the ISCCP B1 archive to be mostly unusable until a rescue effort
72 rectified these issues (Knapp et al. 2007) and provided access to the data for 1983 to present. In
73 addition, further efforts (Knapp 2008b) have expanded the period of record back to 1980.

74 The ISCCP B1 data have since been processed into Gridded Satellite (GridSat) data, a
75 format that is easily accessed and processed by the climate research community at large. This
76 paper describes the construction of the dataset – describing some of the aspects of how the data
77 are provided to facilitate user access – and highlights some of the applications of GridSat. Along
78 the way, the reader is not only encouraged to consider GridSat as a resource for better
79 understanding the Earth’s climate, but also as an example of how other observational data could
80 be provided to a broad user community.

81 **GridSat overview**

82 GridSat data are derived from the ISCCP B1 data, which are detailed by Knapp (2008b).
83 In short, the spatial, temporal, and spectral features of the data are similar to the Hurricane
84 Satellite (HURSAT) dataset (Knapp and Kossin 2007), but at a global scale. The characteristics
85 of the GridSat data are provided in Table 1. The data derive from full-disk images whose scans

86 are closest to the synoptic times: 00, 03, ..., 21 UTC. Primarily, image times begin within 15
87 minutes of the synoptic hour. When data from a synoptic hour are missing, the ISCCP project
88 filled the gap with the best image available closest to that synoptic time.

89 The GridSat dataset is similar to the NOAA Climate Prediction Center (CPC) globally-
90 merged IR product, called the CPC-4km product (Janowiak et al. 2001). This product is created
91 in real-time and used to monitor global precipitation. Because of the similarity between GridSat
92 and CPC-4km, the details of CPC-4km are provided alongside GridSat in Table 1. The primary
93 difference between the two datasets is that the CPC-4km product is geared toward real-time
94 weather and short-term climate applications while GridSat targets long-term global processing.
95 For instance, both datasets attempt to reduce inter-satellite differences by inter-satellite
96 normalization, however, GridSat also performs temporal normalization via calibration against
97 HIRS during the GridSat period of record. Thus, the data are complementary.

98 GridSat data are provided in an equal angle map projection (also called equirectangular
99 or plate carrée), which facilitates the mapping and subsetting of the data. Since the ISCCP B1
100 native resolution is approximately 8km, the resolution of the equal area grid is 0.07° latitude
101 ($\sim 8\text{km}$ at the Equator). The data span the globe in longitude and range from 70°S to 70°N . The
102 spatial and temporal coverage of the satellites contributing to ISCCP B1 is provided in Figure 1 –
103 the so-called “geostationary quilt”. The satellite intercalibration by Knapp (2008a) effectively
104 stitches each quilt piece together, allowing for a consistent global dataset.

105 The satellites included in the GridSat are from agencies that contribute to the ISCCP
106 project. While the first year of GridSat data (1980) is mostly composed of satellites in the
107 GOES-East and West positions (Figure 1b), a four-satellite constellation is representative of the
108 period from 1982 through 1998. (e.g., Figure 1b). Failures of satellites often caused a three-

109 satellite configuration but nearly global coverage is still possible (Figure 1d), though at large
110 view zenith angles. Finally, the Indian Ocean gap was filled in 1998, completing the global
111 coverage (Figure 1e). Figure 1a also demonstrates the international collaboration that resulted in
112 satellite sharing to decrease data gaps, such as when Meteosat 3 was moved west to increase
113 coverage of the Atlantic Ocean in the early 1990s and when GOES 9 was moved to the Pacific
114 Ocean in 2003 to fill the gap between GMS-5 and MTSAT-1R. In recent years, coverage has
115 increased with the provision of the Chinese Feng Yun (FY) geostationary satellites and the loan
116 of GOES satellites for a South American coverage at 60° west.

117 **GridSat Channels**

118 In spite of the diversity of satellites and nations providing data, the ISCCP B1 data
119 provide a uniform set of observations for the infrared window (IR) and visible channels – at 11
120 and 0.6 μm , respectively – during the period of record. Since 1998, the infrared water vapor
121 channel near 6.7 μm is also available on a global basis.

122 The IR channel is a window channel (i.e., a spectral region with little atmospheric
123 absorption) that senses the Earth's surface under clear sky conditions, cloud top temperatures of
124 thick clouds, and a combination of cloud and surface for optically thin clouds or broken clouds
125 within a pixel. Many applications of this channel are discussed below.

126 The visible channel is also a window channel that provides information on clouds and the
127 surface. This channel also has the potential to provide information on Earth radiation budget
128 variables such as aerosols (Knapp 2002) and surface albedo (Loew and Govaerts 2010).

129 The water vapor channels are generally centered near 6.7 μm , which is in a water vapor
130 absorption band making it sensitive to humidity in the upper troposphere. While GridSat water

131 vapor data are temporally too sparse for most atmospheric motion vector applications (where
132 operational products use 30 min data), it can still provide information on some circulation
133 patterns.

134 **Inter-satellite calibration**

135 The data in GridSat use the intercalibration provided by ISCCP calibration efforts
136 (Desormeaux et al. 1993) for the IR and visible channels. The IR channel has also undergone a
137 second intercalibration using the High resolution Infrared Radiation Sounder (HIRS) channel 8
138 as a reference, which detected and corrected bias in the ISCCP calibration at cold temperatures
139 after 2001 (Knapp 2008a).

140 The GridSat IR calibration uncertainty depends on the HIRS calibration as well as the
141 observed differences between HIRS and the geostationary satellites. First, HIRS is a well-
142 calibrated and characterized instrument. Shi et al. (2008) estimate inter-satellite differences for
143 channel 8 to be less than 0.3 K. Furthermore, Cao et al. (2009) report that channel 8 is a good
144 reference channel. Thus, if a sensor is calibrated against HIRS, then it should be quite stable.
145 Second, based on the results of Knapp (2008b), the standard deviation of the monthly mean
146 differences between ISCCP B1 and HIRS provides an estimate of monthly differences while the
147 temporal trend of that bias provides an estimate of the long-term stability. In short, the GridSat
148 IR calibration uncertainty is less than 0.5K for any one satellite with a very stable temporal
149 uncertainty that is less than 0.1 K per decade.

150 The water vapor channel calibration can be tied to a HIRS upper level water vapor
151 channel (band 12) but is complicated by the switch in central wavelength between HIRS/2 to
152 HIRS/3 (from 6.7 to 6.5 μm) and is still being tested.

153 Data are calibrated and stored in GridSat files as brightness temperature (T_b) for
154 longwave channels and reflectance for the visible channel. The IR data are calibrated following
155 Knapp (2008a), view zenith corrected following Joyce et al. (2001) and parallax-corrected
156 following Janowiak et al. (2001).

157 **GridSat Production**

158 For each 3-hour time slot, the channels on each satellite are mapped to an equal-angle
159 grid using nearest-neighbor sampling. Areas of satellite overlap are retained by storing data in
160 layers (see Figure 2). For each channel, the first layer retains observations with the nadir-most
161 (i.e., the lowest) view zenith angle, while a secondary layer holds the regions dropped from the
162 first layer. Similarly, a tertiary layer is retained for the third-best view zenith angles (that are
163 dropped from the secondary layer). The extra layers are provided for future intercomparisons and
164 intercalibrations (i.e., developing algorithms for various zenith angles). Furthermore, a satellite
165 can be reconstructed by combining its contributions to each layer (e.g., by taking all the orange
166 portions from each row of Figure 2, one can reconstruct the GOES-11 full disk image).

167 In addition to the channel data, satellite identification is stored per pixel with
168 corresponding satellite information: satellite latitude, longitude and radius. So while pixel-level
169 satellite view zenith and azimuth angles are not stored, they can be calculated using the Earth
170 location and the stored satellite position (e.g., Soler and Eisemann 1994). Furthermore,
171 calibration information for each channel is provided such that original ISCCP B1 satellite counts
172 can be backed out.

173 Data are stored using netCDF (Rew and Davis 1990) and the Climate and Forecasting
174 (CF) metadata conventions, which facilitates usage with other software (see sidebar). Channel

175 primary layers (nadir-most observation) are written as 2-dimensional (2D) grids in the netCDF
176 file, which facilitates processing of multiple files (e.g., aggregation of multiple times, etc.).
177 Subsequent layers are written as either 2D grids or staggered arrays, which are 1-dimensional
178 arrays that only record data when they exist. Staggered arrays are more efficient when storing
179 maps where data are mostly missing, as is often the case for the tertiary layer.

180 Lastly, in keeping with NRC (2004), who recommend that the capability to reprocess
181 data be incorporated as part of a climate data record program, the GridSat dataset can be
182 reprocessed at NCDC. The entire period of record can be processed in about one week with
183 current computing capabilities. So when new calibration coefficients, navigation adjustments or
184 QC algorithms are developed, the GridSat dataset has the capability to incorporate such
185 improvements. At present, the GridSat data are updated annually, with a goal to update on a
186 monthly basis.

187 **Sidebar: netCDF and CF: Simplifying data access and** 188 **processing**

189 Recent advances in data services allow access and dissemination of data to a broad user
190 community such that data servicing is now more than just putting files on an FTP server. Data
191 servers provide numerous capabilities to users, for example allowing them to download only the
192 data of interest, which saves download bandwidth and research time. Some of the capabilities are
193 summarized below along with a real example of how data processing can be simplified with
194 available tools.

195 The netCDF data format is supported by Unidata and has libraries that allow access to the
196 data from dozens of programming languages. NetCDF version 4.1 also allows for data
197 compression that results in smaller storage and bandwidth requirements. The GridSat data are

198 stored in netCDF using the Climate and Forecasting (CF) convention. In doing so, GridSat data
199 are stored in a manner that other tools recognize. In addition, tools such as the netCDF library
200 and netCDF operators (NCO) (Zender 2008) are capable of reading files across the Internet
201 without previously downloading the data.

202 GridSat data are served using the THREDDS data server (TDS) developed by Unidata,
203 which allows users various options for downloading data. The TDS OPeNDAP access allows an
204 OPeNDAP client (such as the NetCDF library, NCO, IDV and more) to remotely subset and
205 download only the desired data slice or pixel. This provides efficient access to very large files or
206 aggregations (i.e., virtual groups of files) without the user needing to download the entire dataset.
207 The TDS Web Map Service access allows applications such as GIS, Google Earth, or online
208 mapping to directly request rendered images (gif, png, jpeg) from the data server. These images
209 already have a color table applied and can be produced in a variety of predefined projections.
210 The TDS NetCDF Subset Service provides a web-based 'slice-and-dice' service for users. Users
211 may extract a spatial and temporal subset of the data and save the results as CF-compliant
212 NetCDF, XML or comma-separated variable (CSV) text files. Therefore, a variety of user access
213 methods exist that provide interoperability with many existing software tools. Each method can
214 be invoked by a single URL, enabling easy automation and scripting.

215 Numerous tools have been created to simplify the processing of CF compliant data. More
216 than just data visualization, tools like NCO provide command line capabilities to perform
217 averages, concatenations, and more. For instance, sample code is provided in Figure SB1 that
218 processes one month of GridSat IR data, creating diurnally averaged IR Tb over the Sahara
219 Desert for July 2002. Similar code was used to process the global diurnal cycle maps in the
220 outgoing longwave radiation section. The calls to NCO (*ncra* and *ncrcat*) provide a simple

221 means to average IR Tb (via the $-v$ flag) for a specific region (via the $-d$ flag) and concatenate
222 the files together. The alternative would be writing dozens of lines of source code (e.g., C or
223 FORTRAN) to read in the data, calculate the diurnal average, define the output file and write the
224 data. Instead, the seven line shell script accomplishes the same task. The resulting data can then
225 be displayed easily with GrADS (using only 4 commands), for example, to show the mean
226 temperature change from 3 to 15 UTC over the Sahara Desert (Figure SB2).

227 In summary, it is clear that processing gridded netCDF data – such as GridSat – is
228 simplified by the CF convention and the many tools available for serving and processing it.

229 **Dataset applications for infrared window data**

230 Here we present a selection of real-world climatological studies that depend upon
231 GridSat. The aim is to demonstrate the diverse nature of satellite data usage and emphasize the
232 importance of historic satellite data to numerous scientific communities. The applications of
233 GridSat described below are limited to the IR channel data, which has received more extensive
234 inter-satellite calibration. Many of these users are not satellite experts; their research would not
235 have been completed in a timely manner without GridSat.

236 **Tropical cyclones**

237 Given the current questions regarding tropical cyclone variability in a warming climate
238 and the challenges posed by the large uncertainties and heterogeneities in the historical tropical
239 records, one very natural application of GridSat is toward the homogenization of these records.

240 *Tropical disturbances and cyclogenesis*

241 Tropical disturbances are early precursors of tropical cyclones. Traditionally,
242 disturbances have been tracked and evaluated according to the Dvorak technique (Dvorak 1975,

243 1984), which estimates intensity based on the shape and evolution of cloud cover. This technique
244 works best for systems nearing tropical cyclone stage; it is much less effective for weaker
245 systems. To monitor weak systems, surface vector wind information can provide estimates of
246 surface vorticity (Bourassa and McBeth-Ford 2010; Sharp et al. 2002), but coverage from a
247 single scatterometer is insufficient to confidently track tropical disturbances. Therefore, Gierach
248 et al. (2007) combined cloud-top IR observations with the surface vorticity to identify likely
249 tropical disturbances, which proved to be effective for the North Atlantic basin and is being
250 investigated for other tropical cyclone basins using GridSat.

251 Given the limited period of record of scatterometer data, another approach that uses only
252 the IR data to detect potential tropical disturbances has been developed. One requirement for
253 tropical cyclogenesis is the existence of a large area of intense and persistent thunderstorms,
254 called a cloud cluster. Cloud clusters are associated with easterly waves, stalled mid-latitude
255 fronts, and large areas of atmospheric instability. Owing to their critical importance in the
256 tropical cyclogenesis process, recent studies (e.g., Hennon and Hobgood 2003) have manually
257 compiled large datasets of cloud clusters for analysis, a time-consuming task that involves
258 individually examining thousands of basin-wide IR images.

259 In contrast, Hennon et al. (2011) use GridSat IR data to objectively identify cloud
260 clusters, based on a definition by Lee (1989). The process uses a threshold to detect deep
261 convection, and then applies spatial and temporal constraints to determine if the convection is a
262 cloud cluster. Figure 3 shows the frequency of objectively identified cloud cluster tracks for
263 1998-2007. The highest densities are found in the Intertropical and South Pacific convergence
264 zones, North Indian Ocean, and off the west coast of Africa, which are consistent with observed
265 areas of cloud cluster activity and tropical cyclogenesis. The complete cloud cluster dataset spans

266 nearly 30 years and could be applied to several areas of research, including: intraseasonal and
267 interannual studies, impacts of climate change on cloud cluster activity, and case studies for use
268 in tropical cyclogenesis research (e.g., using Knapp et al. 2010).

269 *Estimating cyclone intensity and structure*

270 Tropical cyclones are monitored and forecasted by a number of forecast agencies
271 worldwide. Most forecast agencies provide estimates of the location and intensity of tropical
272 cyclones in their areas of responsibility, but processes and data have improved over time. This
273 makes the historical record of TC intensity heterogeneous by construction. Conversely, studies of
274 the changes to tropical cyclone intensity require data with limited temporal heterogeneities.
275 HURSAT data is the collocation of GridSat with tropical cyclones in the IBTrACS data record
276 (Knapp and Kossin 2007), see Figure 4. TC intensity reanalysis by Kossin et al. (2007a) using
277 HURSAT suggests that the trends in the original TC intensity record are inflated, likely due to
278 changing procedures and capabilities. However, a significant upward trend in the intensity of the
279 strongest storms is still present after correction (Elsner et al. 2008). Additionally, the wind
280 structure inside the tropical cyclone can be derived from HURSAT (Kossin et al. 2007b),
281 providing information about the extent from the storm center that storm force winds reach.

282 *Tropical cyclone transition to extratropical systems*

283 Tropical cyclones moving out of the tropics to the mid-latitudes can undergo significant
284 structural and intensity modifications due to changes in the surrounding large-scale environment:
285 a process termed Extratropical Transition (ET). In general, these tropical systems are weakening
286 as they accelerate poleward over colder sea surface temperatures (or move over land) and into an
287 increasingly baroclinic environment. The ET process is sensitive to the interaction of the

288 decaying tropical cyclone with the atmospheric circulations and underlying ocean/land surface
289 processes over mid-latitudes (Jones et al. 2003). ET events can be tremendous rain makers as the
290 large area of synoptically driven ascent can act on abundant tropical moisture. Numerous studies
291 show that ET is common in all but the eastern Pacific Ocean (Foley and Hanstrum 1994; Hart
292 and Evans 2001; Klein et al. 2000; Sinclair 2002). GridSat, via the HURSAT dataset, is being
293 used to document in detail the remarkable events of late August 1992. During this period, the
294 first ever documented ET in the Eastern Pacific Ocean: Hurricane Lester over the southwestern
295 United States.

296 So in addition to the climatic perspective, GridSat data (via HURSAT) provides an
297 understanding of tropical cyclone conditions throughout their lifetime.

298 **Detection of the ITCZ and its variability on different time scales**

299 GridSat's coverage in the tropics is ideal for the study of larger scale weather features
300 that may exceed the vision of a single geostationary satellite. The ITCZ is one such feature. It
301 occurs as a narrow band spanning the tropics where the trade winds meet, and is visible as a
302 region of increased convective activity. The transient nature of the ITCZ makes accurate
303 detection for process studies challenging. Previous studies used analysis products (e.g.,
304 Magnusdottir and Wang 2008), manually labeled satellite frames and therefore only use a few
305 years of data (e.g., Wang and Magnusdottir 2006), or thresholded Tb to identify the ITCZ
306 (Waliser and Gautier 1993). The latter has the disadvantage of including convection not
307 associated with the ITCZ. Using GridSat data, Bain et. al. (2011) developed a statistical model
308 for ITCZ detection that objectively identifies the envelope of convection. The method requires
309 that the satellite dataset be reliably calibrated over long periods and available at high temporal

310 resolution. GridSat data are ideal for this approach. Figure 5 provides a snapshot of the
311 objectively identified ITCZ in the east Pacific. The area inside the black curve represents the
312 envelope of convection that the statistical model has determined is part of the ITCZ. Note that
313 some isolated convection is not included as part of the ITCZ since it is determined not to be
314 related to the larger scale feature.

315 Using this technique, a database was created identifying the ITCZ in the east Pacific
316 Ocean (90 - 180W, 0 - 30N) every 3 hours from 1980 to 2008. The database has been used to
317 construct detailed analysis of the variability of the ITCZ on interannual and intraseasonal time
318 scales (Bain et al. 2011). The additional advantage of the high temporal sampling has also
319 allowed in-depth studies of the diurnal cycle of the ITCZ (Bain et al. 2010), where the ITCZ size,
320 as well as the character of clouds within in it, were found to vary according to time of day. The
321 ability to use the same dataset for both short timescales and long timescales lends strength to
322 investigations of the ITCZ and is therefore particularly useful for relating climatological and
323 dynamical aspects of the feature.

324 **Precipitation**

325 The detection of precipitation is not wholly unrelated to the above applications, as both
326 tropical cyclones and the ITCZ can cause copious amounts of precipitation. The following details
327 the study of precipitation using GridSat at global and regional scales.

328 *Global precipitation climatologies*

329 The Global Precipitation Climatology Project (GPCP), an international community
330 activity of GEWEX under the World Climate Research Program (WCRP), provides long-term
331 global estimates of monthly and daily precipitation (Adler et al. 2003; Huffman et al. 2001).

332 Previous and current GPCP algorithms use compilations of merged geostationary IR Tb whose
333 period of record, latitudinal extent, and time/space resolution hamper computations. A new
334 version of the GPCP datasets is now in development, with GridSat-B1 data as one key upgrade.
335 Based on the contribution of GridSat, it is anticipated that the monthly product will be shifted
336 from the current 2.5° grid to 0.5°, while the daily will shift from 1° to 0.25°. In addition, the
337 daily dataset eventually could be pushed from its current start of October 1996, perhaps to the
338 start of Special Sensor Microwave Imager data in July 1987. For both datasets, the current
339 latitude bounds for geostationary IR data of 40N-40S will be relaxed to the entire useful range of
340 simple IR-based estimates, around 50-deg in the summer hemisphere.

341 In addition to these traditional precipitation climatologies, GridSat also facilitates
342 research on precipitation detection. For instance, GridSat provides complementary information at
343 high temporal and spatial resolution for three different channels. The high spatial resolution of
344 GridSat can help to better identify cloud systems capable of producing rain while the high
345 temporal resolution allows for tracking the development and movement of medium- and large-
346 scale cloud systems. The data from the IR channel can be used to better identify convective cells
347 and therefore resolve precipitating systems with a scale smaller than the footprint of a microwave
348 sensor [similar to the approach of Joyce et al. (2004)]. Merging the multi-spectral and high
349 resolution GridSat data with data from sensors on polar orbiting satellites might be a fruitful
350 pursuit, which could allow for temporal interpolation between subsequent overpasses of a
351 microwave sensor that only provide a few observations per day at a global scale.

352 Erroneous discrimination of optically thin and thick clouds can have a significant effect
353 on uncertainties in precipitation retrieval (Ba and Gruber 2001). Non-precipitating cirrus clouds
354 mistakenly interpreted as thick precipitating clouds contribute to overestimation of rain rate.

355 Differencing between GridSat IR window and water vapor channels allows one to discriminate
356 between optically thin clouds and thick clouds possibly overlaid by cold ice clouds (Turk and
357 Miller 2005). Thus, GridSat data will likely have a significant impact on improved global
358 precipitation climatologies.

359 *Mercury wet deposition: Polluted rain*

360 At regional scales, Holmes (2008; 2011) applied GridSat data to the study of societal
361 impacts of precipitation in the eastern United States. Wet deposition is a major source of mercury
362 to ecosystems, which can be harmful to fish, birds and humans (Lindberg et al. 2007; Mergler et
363 al. 2007; Scheuhammer et al. 2007). For example, fish in many US water bodies have mercury
364 concentrations considered unsafe for consumption, motivating efforts to understand and reduce
365 mercury exposure through precipitation.

366 Mercury deposition in the southeast US is nearly double that in the northeast (Figure 6a)
367 despite lower anthropogenic emissions in the region (Environmental Protection Agency 2008;
368 Mercury Deposition Network 2006). Peak seasonal deposition occurs in summer when
369 convective storms are common. This led Guentzel et al. (2001) and Selin and Jacob (2008) to
370 hypothesize a causal link between high-altitude wet scavenging in deep convection and the
371 elevated deposition. Holmes (2008; 2011) tested this hypothesis by correlating IR cloud
372 temperatures from GridSat with mercury deposition measured by the EPA Mercury Deposition
373 Network (MDN). Precipitation samples accumulate over one week and the associated cloud
374 temperatures are calculated as the average over the collection period of daily minimum
375 temperatures observed within 20 km of the collection site. Deposition clearly increases with
376 colder temperatures (Figure 6b), but this is partially due to large precipitation depths associated

377 with tall, cold clouds. Figure 6c shows that even for equivalent rainfall depths, mercury
378 deposition is about 2 times greater in the samples with the coldest average clouds ($T_b < 240$ K)
379 compared with the warmest ones ($T_b > 260$ K). Ongoing work addresses the dynamical
380 implications of these results.

381 **Precipitation and temperature monitoring in data sparse regions**

382 Another societal implication of precipitation is the availability of food production in
383 regions with little irrigation infrastructure, where adverse trends in rainfall and temperature can
384 disrupt agriculture and pastoral livelihoods. Our understanding of where rainfall declines or
385 temperature increases exacerbate food security has been limited by sparse *in situ* data. Therefore,
386 the US Agency for International Development Famine Early Warning Systems Network (FEWS
387 NET) has supported the creation and analysis of rainfall and temperature climatologies in food
388 insecure regions. FEWS NET has begun working extensively with the GridSat data in order to
389 make finer resolution maps of rainfall and air temperatures over a thirty-year period.

390 Spatial analysis of GridSat IR T_b percentiles are used over a 4-month period to estimate
391 mean temperature and total precipitation based on correlation with the sparse *in situ* sites. For
392 algorithm details, see Funk et al. (2012). The mean 1999-2008 June-September temperature field
393 is in the top-left of Figure 7. High mountainous areas in Kenya, Ethiopia and near the border of
394 Cameroon and Nigeria are cool, while the sands of the Sahara and the Afar region of Ethiopia are
395 very warm. Long-term variations can be mapped by looking at decadal differences (between two
396 decades: 1984-1993 and 1999-2008).

397 Looking at the temperature changes (Figure 7, bottom left), a substantial warming signal
398 is apparent, which also appears in the station data. Spatially, however, the strongest warming

399 (>1° C since 1984-1993) appears across a coherent area stretching from Western Kenya and
400 Ethiopia across the Zaire basin. June-September rainfall, on the other hand, exhibits an increase
401 across northern Ethiopia and most of the Sahel. Decreases are found across eastern Ethiopia,
402 most of Kenya and Uganda, and the Zaire basin. The spatial detail of these maps should help us
403 understand and adapt to decadal climate variations. Such differences may relate to climate
404 change or may be simply due to inherent climate variability. In either case, decadal fluctuations
405 can impact food security, hydrological resources, and environmental sustainability. The GridSat
406 data help us capture shifts in temperature and precipitation, building a high resolution picture of
407 change. While the GridSat-enhanced analyses are still evolving, it seems likely that these data
408 will substantially improve our ability to track rainfall and temperature changes, enhancing our
409 ability to adapt in a changing world.

410 **Outgoing Longwave Radiation**

411 The Earth radiation budget describes the distribution of radiative energy in the Earth-
412 atmosphere system. The observations of Earth radiation budget parameters at the top of the
413 atmosphere have been performed from both operational and experimental satellites since the
414 1970s. The long and continuous time series of Earth radiation budget parameters, e.g., the
415 outgoing longwave radiation (OLR), is valuable for climate change studies and monitoring. Polar
416 orbiting satellites provide fairly uniform spatial and angular sampling from a given instrument,
417 but with relatively poor temporal sampling resolution. GridSat data provide information on the
418 diurnal variation that is essential for deriving the OLR time series accurately.

419 The HIRS OLR climate data record was generated with a set of climatological OLR
420 diurnal models (Lee et al. 2007) that help to reduce the monthly OLR errors resulting from the

421 orbital drift of polar-orbiting satellites. Although these models are self-consistent with the HIRS
422 OLR retrievals, for error budgeting purposes, we would like to assess whether these diurnal
423 models were truly representative and how significant the inter-annual variations can be. Figure 8
424 shows the comparison of the HIRS climatological OLR diurnal models for August 2002 with
425 those derived from the GridSat IR data. Some disagreements are apparent for certain
426 regions/climate types. Nevertheless, for the majority, they seem to share a high degree of
427 similarity, both in shape and in phase. These results provide us confidence in the quality and
428 guidance for future improvement of the OLR climate data record production. Similar
429 comparisons are necessary for other seasons and years.

430 A hybrid OLR product can then be generated using HIRS observations and GridSat
431 following Lee et al. (2004). Such a combination would take advantage of both the accuracy of
432 the HIRS OLR retrieval and the precise diurnal variation signal in GridSat. This product will
433 improve the temporal integral accuracy for the HIRS climate data record and possibly allow
434 product generation at a temporal resolution finer than monthly, which would benefit dynamical
435 diagnostic applications.

436 **Future Work**

437 **Future applications using visible and water vapor channels**

438 The bulk of the above applications focused on the IR channel, however many areas of
439 study exist for the global inter-calibrated visible and water vapor channels. The visible channel is
440 sensitive to clouds and in some regions aerosols as well. Aerosols have a significant role in our
441 daily lives by affecting human health and in our understanding of the Earth's radiation budget
442 via the uncertainty in how much solar radiation they reflect to space versus absorb (in addition to

443 how they affect cloud optical properties and lifetime). Knapp (2002) defined a means to detect
444 the aerosol signal in satellite observations. When this technique is applied to visible GridSat data,
445 many ground sites – Aerosol Robotic Network sites (Holben et al. 1998) – show a strong aerosol
446 signal that implies (given a good cloud algorithm) aerosols can be retrieved from GridSat.

447 GridSat data also have the potential to help accurately determine shortwave and
448 longwave radiative fluxes at the regional to global scale. The Earth’s surface albedo is a key
449 terrestrial variable in these flux calculations. While surface albedo data are available from the
450 MODIS sensor since 2000 (Schaaf et al. 2002), long term surface albedo data products that cover
451 multiple decades previously could only rely on operational weather satellites that were not
452 designed for climate monitoring. The potential to derive global maps of surface albedo from
453 mosaics of geostationary observations has been shown by Govaerts et al. (2008) and the GridSat
454 data might be used for the retrieval of global fields of surface albedo in this way.

455 The water vapor channel provides information on energetics of the upper troposphere.
456 The channel is sensitive to a broad region of upper tropospheric humidity that can provide
457 information on the distribution and transport of water vapor in the troposphere (Soden and
458 Bretherton 1993; Tian et al. 2004). This channel also has the potential to provide information on
459 water vapor entering the stratosphere (Schmetz et al. 1997) via overshooting convective clouds.
460 In such cases, the water vapor channel can be warmer than the IR channel for convection that
461 penetrates the tropopause. GridSat data – in providing global coverage for both channels – has
462 the potential to help monitor the transport of water vapor.

463 **Dataset improvements**

464 Given the widespread use of GridSat data, efforts are underway to further improve the
465 dataset. The ISCCP project is revamping software processing to produce higher resolution cloud
466 products based on ISCCP B1 data. As part of this work, the pixel-level cloud mask will be
467 incorporated into GridSat, providing information on the presence of clouds in the GridSat data.

468 Furthermore, the use of GridSat data by non-satellite experts suggests that a similar
469 remapping of other satellite data would benefit more scientists. For example, instruments on
470 polar orbiting satellites could be remapped in a similar way. This would make data – like that
471 from AVHRR, HIRS and other instruments – more widely available to a broad base of users.

472 In the future, the GridSat data will incorporate better calibration as it becomes available.
473 In particular, the WMO Global Space-based Inter Calibration System (GSICS) is working to
474 inter-calibrate sensors on all meteorological satellites. However, the initial GSICS priority is to
475 process operational sensors. Furthermore, their current method is to calibrate against space-based
476 hyper-spectral radiometers, thus limiting their reprocessing efforts to starting in 2002. The
477 GSICS effort to re-calibrate historical sensors (prior to 2002) has not yet begun. Nonetheless, the
478 GridSat dataset will be reprocessed as needed to be consistent with GSICS and the NOAA CDR
479 program.

480 Lastly, the observations that comprise the GridSat data are being revised. The visible and
481 water vapor radiances will soon be inter-calibrated. The IR satellite view zenith angle correction
482 could be improved as well because the current algorithm (Joyce et al. 2001) was developed for
483 satellites in use in 2000 (GOES-8,10, GMS-5, Meteosat-5,7). However, the corrections are likely
484 satellite dependent, particularly because the older satellites had more water vapor contamination

485 in the infrared window channels. An updated satellite zenith angle correction that is satellite
486 dependent would decrease the remnant seams still apparent in GridSat IR data.

487 **Summary**

488 Geostationary satellites have now been providing weather data for 50 years. Much of
489 these data have been neglected by climate observation studies due to difficulties with calibration
490 and data processing over such a long period. Collection and data ownership rights were spread
491 out across several international agencies. The ISCCP project is overcoming these barriers and
492 this paper has presented details on the most up-to-date and easily accessible global satellite
493 record: GridSat.

494 This new record provides equal-angle gridded uniform observations of brightness
495 temperatures every 3 hours from 1980 to the present for most of the globe. We have
496 demonstrated the multiple and diverse uses of the data for climate analysis made possible by
497 GridSat data – from predicting drought and food security in Africa to the detailed and historical
498 tracking of hurricanes. This only touches on some of the potential uses of GridSat. Accurate
499 records of global atmospheric fields are essential for future research on climate change as well as
500 the understanding of the planet’s meteorology.

501 By reconstructing past satellite data and combining them with current satellite
502 observations, a seamless data record has been obtained for the study of the Earth’s atmospheric
503 state. In addition, GridSat has given a wide range of users very easy access to this new data
504 record. Development of GridSat will continue, focusing on improving the current data files and
505 supporting more applications.

506 **Acknowledgements**

507 K. Knapp acknowledges the significant contribution of George Huffman in the design of the
508 GridSat dataset. Many were integral in the initial rescue of the ISCCP B1 data, including Bill
509 Rossow, John Bates, Garrett Campbell and many at the agencies that provided the B1 data: JMA,
510 EUMETSAT and NOAA. A. Loew acknowledges the support of the Cluster of Excellence
511 'CliSAP' (EXC177), University of Hamburg. Any use of trade, product, or firm names is for
512 descriptive purposes only and does not imply endorsement by the U.S. Government.

513 **References**

- 514 Adler, R. F., and Coauthors, 2003: The Version-2 Global Precipitation Climatology Project
515 (GPCP) Monthly Precipitation Analysis (1979-Present). *Journal of Hydrometeorology*, **4**,
516 1147-1167.
- 517 Ba, M. B., and A. Gruber, 2001: GOES Multispectral Rainfall Algorithm (GMSRA). *Journal of*
518 *Applied Meteorology*, **40**, 1500-1514.
- 519 Bain, C. L., G. Magnusdottir, P. Smyth, and H. Stern, 2010: Diurnal cycle of the Intertropical
520 Convergence Zone in the east Pacific. *Journal of Geophysical Research*, **115**, D23116.
- 521 Bain, C. L., J. De Paz, J. Kramer, G. Magnusdottir, P. Smyth, H. Stern, and C.-C. Wang, 2011:
522 Detecting the ITCZ in instantaneous satellite data using spatial-temporal statistical
523 modeling: ITCZ climatology in the east Pacific. *Journal of Climate*, **24**, 216-230.
- 524 Bourassa, M. A., and K. McBeth-Ford, 2010: Uncertainty in Scatterometer-Derived Vorticity.
525 *Journal of Atmospheric and Oceanic Technology*, **27**, 594-603.
- 526 Cao, C., M. Goldberg, and L. Wang, 2009: Spectral Bias Estimation of Historical HIRS Using
527 IASI Observations for Improved Fundamental Climate Data Records. *Journal of*
528 *Atmospheric and Oceanic Technology*, **26**, 1378-1387.

529 Desormeaux, Y., W. B. Rossow, C. L. Brest, and G. G. Campbell, 1993: Normalization and
530 Calibration of Geostationary Satellite Radiances for the International Satellite Cloud
531 Climatology Project. *Journal of Atmospheric and Oceanic Technology*, **10**, 304-325.

532 Dvorak, V. F., 1975: Tropical Cyclone Intensity Analysis and Forecasting from Satellite
533 Imagery. *Monthly Weather Review*, **103**, 420-430.

534 Dvorak, V. F., 1984: *Tropical cyclone intensity analysis using satellite data*. National Oceanic
535 and Atmospheric Administration, National Environmental Satellite, Data, and
536 Information Service, 47 pp.

537 Elsner, J. B., J. P. Kossin, and T. H. Jagger, 2008: The increasing intensity of the strongest
538 tropical cyclones. *Nature*, **455**, 92-95.

539 Environmental Protection Agency, 2008: Model-based analysis and tracking of airborne mercury
540 emissions to assist in watershed planning. *United States Environmental Protection*
541 *Agency*, 350 pp.

542 Foley, G. R., and B. N. Hanstrum, 1994: The Capture of Tropical Cyclones by Cold Fronts off
543 the West Coast of Australia. *Weather and Forecasting*, **9**, 577-592.

544 Funk, C., J. C. Michaelsen, and M. Marshall, 2012: Mapping recent decadal climate variations in
545 Eastern Africa and the sahel. *Remote Sensing of Drought: Innovative Monitoring*
546 *Approaches*, B. Wardlow, and M. Anderson, Eds.

547 Gierach, M. M., M. A. Bourassa, P. Cunningham, J. J. O'Brien, and P. D. Reasor, 2007:
548 Vorticity-Based Detection of Tropical Cyclogenesis. *Journal of Applied Meteorology and*
549 *Climatology*, **46**, 1214-1229.

550 Govaerts, Y. M., A. Lattanzio, M. Taberner, and B. Pinty, 2008: Generating global surface
551 albedo products from multiple geostationary satellites. *Remote Sensing of Environment*,
552 **112**, 2804-2816.

553 Guentzel, J. L., W. M. Landing, G. A. Gill, and C. D. Pollman, 2001: Processes Influencing
554 Rainfall Deposition of Mercury in Florida. *Environmental Science & Technology*, **35**,
555 863-873.

556 Hart, R. E., and J. L. Evans, 2001: A Climatology of the Extratropical Transition of Atlantic
557 Tropical Cyclones. *Journal of Climate*, **14**, 546-564.

558 Hennon, C. C., and J. S. Hobgood, 2003: Forecasting Tropical Cyclogenesis over the Atlantic
559 Basin Using Large-Scale Data. *Monthly Weather Review*, **131**, 2927-2940.

560 Hennon, C. C., C. N. Helms, K. R. Knapp, and A. R. Bowen, 2011: An Objective Algorithm for
561 Detecting and Tracking Tropical Cloud Clusters: Implications for Tropical Cyclogenesis
562 Prediction. *Journal of Atmospheric and Oceanic Technology*, **In press**.

563 Holben, B. N., and Coauthors, 1998: AERONET - A federated instrument network and data
564 archive for aerosol characterization. *Remote Sensing of the Environment*, **66**, 1-16.

565 Holmes, C. D., 2008: Mercury deposition to the Gulf Coast region from deep convection and
566 long-range atmospheric transport. *AGU Fall Meeting*, San Francisco, CA, Eos
567 Transactions.

568 Holmes, C. D., and Coauthors, 2011: Thunderstorms explain high mercury deposition in the
569 Southeast United States, **In preparation**.

570 Huffman, G. J., R. F. Adler, M. M. Morrissey, D. T. Bolvin, S. Curtis, R. Joyce, B. McGavock,
571 and J. Susskind, 2001: Global Precipitation at One-Degree Daily Resolution from
572 Multisatellite Observations. *Journal of Hydrometeorology*, **2**, 36-50.

573 Janowiak, J. E., R. J. Joyce, and Y. Yarosh, 2001: A real-time global half-hourly pixel-resolution
574 infrared dataset and its applications. *Bulletin of the American Meteorological Society*, **82**,
575 205-217.

576 Jones, S. C., and Coauthors, 2003: The Extratropical Transition of Tropical Cyclones: Forecast
577 Challenges, Current Understanding, and Future Directions. *Weather and Forecasting*, **18**,
578 1052-1092.

579 Joyce, R., J. Janowiak, and G. Huffman, 2001: Latitudinally and Seasonally Dependent Zenith-
580 Angle Corrections for Geostationary Satellite IR Brightness Temperatures. *Journal of*
581 *Applied Meteorology*, **40**, 689-703.

582 Joyce, R. J., J. E. Janowiak, P. A. Arkin, and P. Xie, 2004: CMORPH: A Method that Produces
583 Global Precipitation Estimates from Passive Microwave and Infrared Data at High
584 Spatial and Temporal Resolution. *Journal of Hydrometeorology*, **5**, 487-503.

585 Klein, P. M., P. A. Harr, and R. L. Elsberry, 2000: Extratropical Transition of Western North
586 Pacific Tropical Cyclones: An Overview and Conceptual Model of the Transformation
587 Stage. *Weather and Forecasting*, **15**, 373-395.

588 Knapp, K. R., 2002: Quantification of aerosol signal in GOES-8 visible imagery over the U.S.
589 *Journal of Geophysical Research*, **107**, 10.1029/2001JD002001.

590 Knapp, K. R., 2008a: Calibration of long-term geostationary infrared observations using HIRS.
591 *Journal of Atmospheric and Oceanic Technology*, **25**, 183-195.

592 Knapp, K. R., 2008b: Scientific data stewardship of International Satellite Cloud Climatology
593 Project B1 global geostationary observations. *Journal of Applied Remote Sensing*, **2**,
594 023548

595 Knapp, K. R., and J. P. Kossin, 2007: New global tropical cyclone data from ISCCP B1
596 geostationary satellite observations. *Journal of Applied Remote Sensing*, **1**, 013505

597 Knapp, K. R., J. J. Bates, and B. Barkstrom, 2007: Scientific Data Stewardship: Lessons learned
598 from a satellite data rescue effort. *Bulletin of the American Meteorological Society*, **88**,
599 1359-1361.

600 Knapp, K. R., M. C. Kruk, D. H. Levinson, H. J. Diamond, and C. J. Neumann, 2010: The
601 International Best Track Archive for Climate Stewardship (IBTrACS): Centralizing
602 tropical cyclone best track data. *Bulletin of the American Meteorological Society*, **91**,
603 363-376.

604 Kossin, J. P., K. R. Knapp, D. J. Vimont, R. J. Murnane, and B. A. Harper, 2007a: A globally
605 consistent reanalysis of hurricane variability and trends. *Geophysical Research Letters*,
606 **34**, L04815.

607 Kossin, J. P., J. A. Knaff, H. I. Berger, D. C. Herndon, T. A. Cram, C. S. Velden, R. J. Murnane,
608 and J. D. Hawkins, 2007b: Estimating hurricane wind structure in the absence of aircraft
609 reconnaissance. *Weather and Forecasting*, **22**, 89-101.

610 Lee, C. S., 1989: Observational Analysis of Tropical Cyclogenesis in the Western North Pacific.
611 Part I: Structural Evolution of Cloud Clusters. *Journal of Atmospheric Science*, **46**, 2580-
612 2598.

613 Lee, H.-T., A. K. Heidinger, A. Gruber, and R. G. Ellingson, 2004: The HIRS Outgoing
614 Longwave Radiation product from hybrid polar and geosynchronous satellite
615 observations. *Advances in Space Research*, **33**.

616 Lee, H.-T., A. Gruber, R. G. Ellingson, and I. Laszlo, 2007: Development of the HIRS Outgoing
617 Longwave Radiation climate data set. *Journal of Atmospheric and Oceanic Technology*,
618 **24**, 2029-2047.

619 Lindberg, S., and Coauthors, 2007: A Synthesis of Progress and Uncertainties in Attributing the
620 Sources of Mercury in Deposition. *AMBIO: A Journal of the Human Environment*, **36**,
621 19-33.

622 Loew, A., and Y. Govaerts, 2010: Towards Multidecadal Consistent Meteosat Surface Albedo
623 Time Series. *Remote Sensing*, **2**, 957-967.

624 Magnusdottir, G., and C.-C. Wang, 2008: Intertropical Convergence Zones during the Active
625 Season in Daily Data. *Journal of Atmospheric Science*, **65**, 2425-2436.

626 Mercury Deposition Network, 2006: National Atmospheric Deposition Program 2005 Annual
627 Summary. 16 pp.

628 Mergler, D., H. A. Anderson, L. H. M. Chan, K. R. Mahaffey, M. Murray, M. Sakamoto, and A.
629 H. Stern, 2007: Methylmercury Exposure and Health Effects in Humans: A Worldwide
630 Concern. *AMBIO: A Journal of the Human Environment*, **36**, 3-11.

631 National Research Council, 2004: Climate Data Records from Environmental Satellites, 116 pp.

632 Rew, R., and G. Davis, 1990: NetCDF: an interface for scientific data access. *Computer
633 Graphics and Applications, IEEE*, **10**, 76-82.

634 Reynolds, R. W., N. A. Rayner, T. M. Smith, D. C. Stokes, and W. Wang, 2002: An Improved In
635 Situ and Satellite SST Analysis for Climate. *Journal of Climate*, **15**, 1609-1625.

636 Schaaf, C. B., and Coauthors, 2002: First operational BRDF, albedo nadir reflectance products
637 from MODIS. *Remote Sensing of Environment*, **83**, 135-148.

638 Scheuhammer, A. M., M. W. Meyer, M. B. Sandheinrich, and M. W. Murray, 2007: Effects of
639 Environmental Methylmercury on the Health of Wild Birds, Mammals, and Fish.
640 *AMBIO: A Journal of the Human Environment*, **36**, 12-19.

641 Schmetz, J., S. A. Tjemkes, M. Gube, and L. van de Berg, 1997: Monitoring deep convection
642 and convective overshooting with METEOSAT. *Advances in Space Research*, **19**, 433-
643 441.

644 Selin, N. E., and D. J. Jacob, 2008: Seasonal and spatial patterns of mercury wet deposition in
645 the United States: Constraints on the contribution from North American anthropogenic
646 sources. *Atmospheric Environment*, **42**, 5193-5204.

647 Sharp, R. J., M. A. Bourassa, and J. J. O'Brien, 2002: Early Detection of Tropical Cyclones
648 Using Seawinds-Derived Vorticity. *Bulletin of the American Meteorological Society*, **83**,
649 879-889.

650 Shi, L., J. J. Bates, and C. Cao, 2008: Scene radiance-dependent intersatellite biases of HIRS
651 longwave channels. *Journal of Atmospheric and Oceanic Technology*, **25**, 2219-2229.

652 Sinclair, M. R., 2002: Extratropical Transition of Southwest Pacific Tropical Cyclones. Part I:
653 Climatology and Mean Structure Changes. *Monthly Weather Review*, **130**, 590-609.

654 Soden, B. J., and F. P. Bretherton, 1993: Upper Tropospheric Relative Humidity From the GOES
655 6.7 μm Channel: Method and Climatology for July 1987. *J. Geophys. Res.*, **98**, 16669-
656 16688.

657 Soler, T., and D. W. Eisemann, 1994: Determination of look angles to geostationary
658 communication satellites. *J. Surv. Eng. ACSE*, **120**, 115-127.

659 Tian, B. J., B. J. Soden, and X. Q. Wu, 2004: Diurnal cycle of convection, clouds, and water
660 vapor in the tropical upper troposphere: Satellites versus a general circulation model.
661 *Journal of Geophysical Research-Atmospheres*, **109**, D10101.

662 Turk, F. J., and S. D. Miller, 2005: Toward improved characterization of remotely sensed
663 precipitation regimes with MODIS/AMSR-E blended data techniques. *IEEE*
664 *Transactions on Geoscience and Remote Sensing*, **43**, 1059-1069.

665 Waliser, D. E., and C. Gautier, 1993: A Satellite-derived Climatology of the ITCZ. *Journal of*
666 *Climate*, **6**, 2162-2174.

667 Wang, C.-C., and G. Magnusdottir, 2006: The ITCZ in the Central and Eastern Pacific on
668 Synoptic Time Scales. *Monthly Weather Review*, **134**, 1405-1421.

669 Zender, C. S., 2008: Analysis of self-describing gridded geoscience data with netCDF Operators
670 (NCO). *Environmental Modelling & Software*, **23**, 1338-1342.

671

672

673

674 **Figure Captions**

675 Figure 1 – a) Time series of ISCCP B1 geostationary satellite coverage at the Equator (limited to
676 a view zenith angle of 60° for illustrative purposes). b-e) Sample GridSat coverage for typical
677 satellite coverages: b) Two-satellite coverage with only GOES-East and -West in 1980, c) Four-
678 satellite coverage that is typical of most of the period 1982-1998, d) typical three-satellite
679 coverage when the U.S. was operating only one satellite (e.g., 1985-1987 or 1989-1992) and e)
680 five-satellite coverage that is typical of the current era (1998 to present).

681 Figure 2 - Merged GridSat IR image from 1 Jan. 2008 (left) alongside identification of the
682 satellites used to construct the IR image (right). The satellites FY-2C (red), GOES-11 (orange),
683 GOES-12 (yellow), Meteosat-7 (green), Meteosat-9 (blue), and MTSAT-1R (violet) are used.
684 Black regions denote missing data. The top row is the nadir-most set of observations.
685 Observations and satellites in the 2nd row are those not used in the top row due to larger view
686 zenith angles. The 3rd row consequently represents those observations eliminated from the 2nd
687 row.

688 Figure 3 – Cloud cluster frequency (clusters per year within 55km of any point) for the first
689 decade of global satellite coverage (1998-2007). Contour levels are set at 1, 5 and 10 per year.

690 Figure 4 - HURSAT image of 1992 Hurricane Andrew from August 23, 1992 along with a time
691 series of its maximum sustained wind (in knots).

692 Figure 5 - Example of ITCZ detection in the east Pacific using the statistical model for 18
693 August 2000 at 2100 UTC. The grayscale represents IR temperature (K) from GridSat; the black
694 line outlines the identified location of the ITCZ. The North American coastline is outlined in
695 white.

696 Figure 6 - (A) Mercury wet deposition in the eastern United States for 2005. Stars show sites
697 analyzed here. (B) Mercury wet deposition for summers 2001-2006 and mean infrared (IR) cloud
698 temperature from GridSat IR. (C) Mercury wet deposition and precipitation for three different
699 cloud temperature ranges. Lines show mean concentration in 50 mm precipitation bins for the
700 coldest (temperature $< 240\text{K}$) and warmest (temperature $> 260\text{K}$) clouds. [Figures adapted from
701 (Holmes 2008; Holmes et al. 2011)(Mercury Deposition Network 2006)]

702 Figure 7 – June-September (JJAS) air temperature and rainfall estimates based on combinations
703 of GridSat infrared fields and in situ station observations. The top two panels show decadal
704 average air temperature (left) and rainfall (right) for the 1999-2008 period. The bottom panels
705 show the differences between these decadal averages and the 1984-1993 average (the 1999-2008
706 average minus the 1984-1993 average).

707 Figure 8 - Comparison of diurnal OLR models from the HIRS climatology and GridSat for
708 August 2002. The GridSat OLR helps to verify the representativeness of the climatological OLR
709 diurnal models used in the production of the HIRS OLR climate data record. The arrows in the
710 central panel indicate the phases of the OLR diurnal models with the 12 o'clock local time
711 pointing north, running counter-clockwise. The surrounding plots compare the diurnal models
712 for selected regions with distinctively different types of diurnal variations. The mean values of
713 GridSat OLR in each diurnal plot were adjusted to those of the HIRS to aid visual comparison.
714

715

716 **Tables**

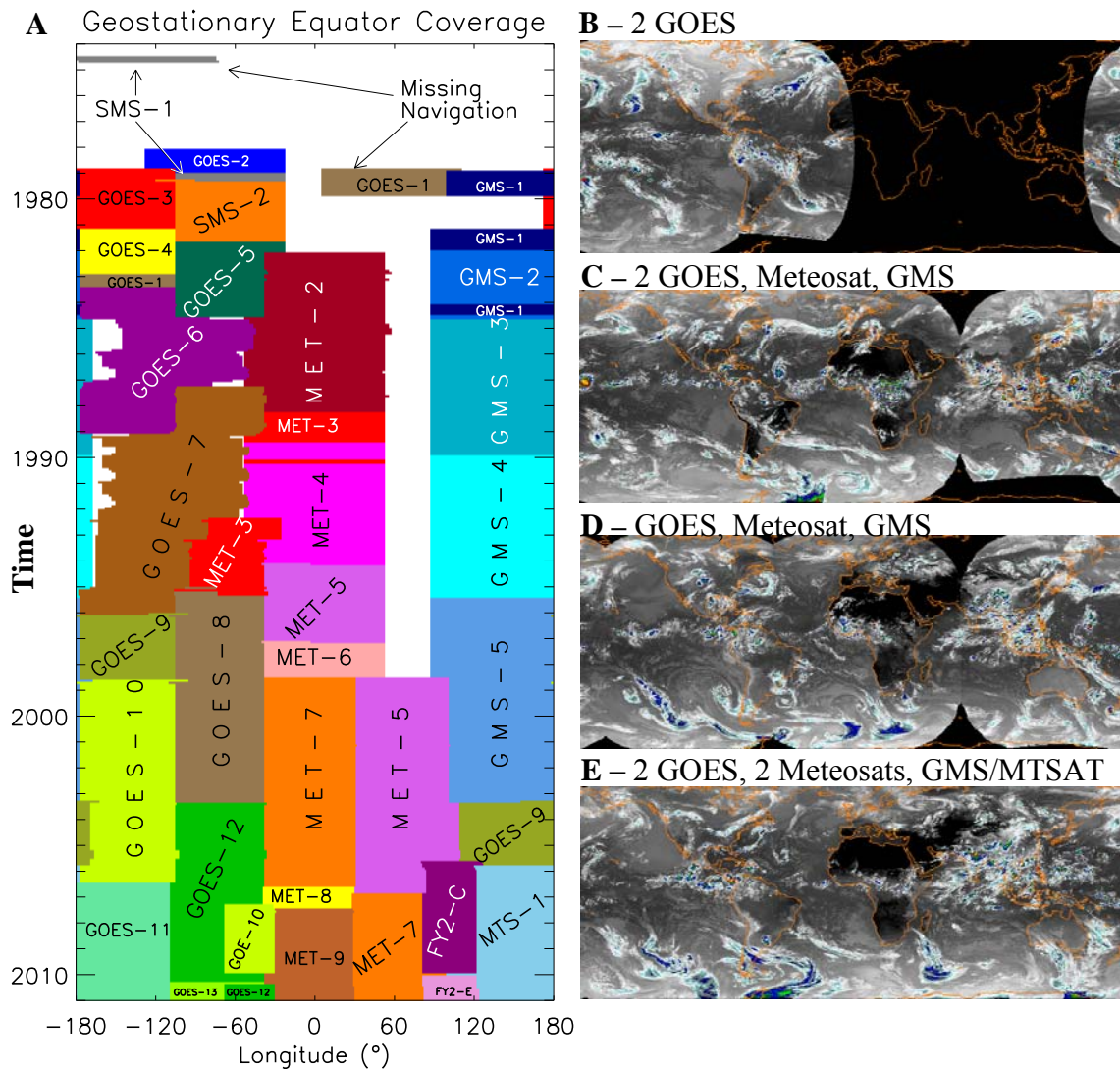
717 Table 1 - Summary of similarities and differences between the CPC-4km product and the

718 GridSat dataset.

	CPC-4km	GridSat
Spatial resolution	4km	8km
Temporal resolution	30 min	180 min
Channels	1 (IR)	3 (IR, water vapor, visible)
Monthly Volume <i>(uncompressed)</i>	45 GB	40 GB
Period of record	2000-present	1980-present
Inter-satellite normalization	Yes	Yes
Temporal normalization	No	Yes
Format	Unformatted binary	netCDF

719

720 **Figures**



721

722 Figure 1 – a) Time series of ISCCP B1 geostationary satellite coverage at the Equator (limited to

723 a view zenith angle of 60° for illustrative purposes). b-e) Sample GridSat coverage for typical

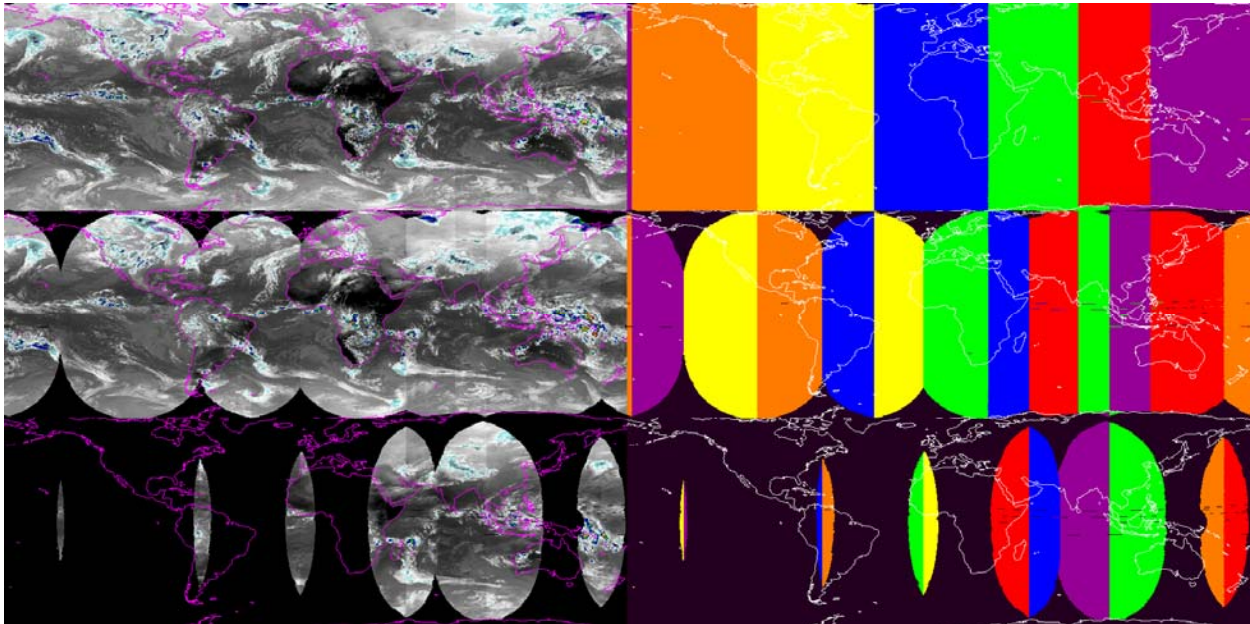
724 satellite coverages: b) Two-satellite coverage with only GOES-East and -West in 1980, c) Four-

725 satellite coverage that is typical of most of the period 1982-1998, d) typical three-satellite

726 coverage when the U.S. was operating only one satellite (e.g., 1985-1987 or 1989-1992) and e)

727 five-satellite coverage that is typical of the current era (1998 to present).

728



729

730 Figure 2 - Merged GridSat IR image from 1 Jan. 2008 (left) alongside identification of the
731 satellites used to construct the IR image (right). The satellites FY-2C (red), GOES-11 (orange),
732 GOES-12 (yellow), Meteosat-7 (green), Meteosat-9 (blue), and MTSAT-1R (violet) are used.
733 Black regions denote missing data. The top row is the nadir-most set of observations.
734 Observations and satellites in the 2nd row are those not used in the top row due to larger view
735 zenith angles. The 3rd row consequently represents those observations eliminated from the 2nd
736 row.

737 **SWF/GIF**

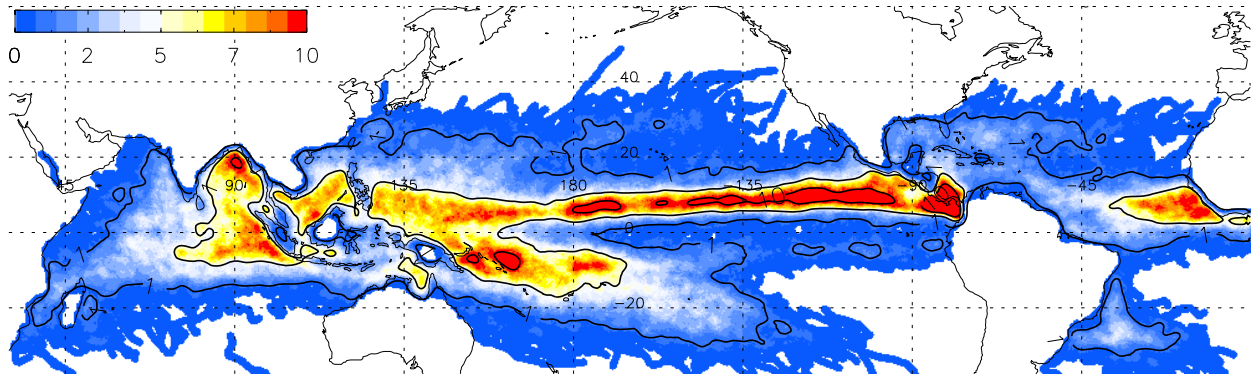
738 Animation location:

739 ftp://eclipse.ncdc.noaa.gov/pub/misc/kknapp/bams_grisat/GriSat-Construction.gif or

740 ftp://eclipse.ncdc.noaa.gov/pub/misc/kknapp/bams_grisat/GridSat-Construction.swf

741

742



743

744 Figure 3 – Cloud cluster frequency (clusters per year within 55km of any point) for the first
745 decade of global satellite coverage (1998-2007). Contour levels are set at 1, 5 and 10 per year.

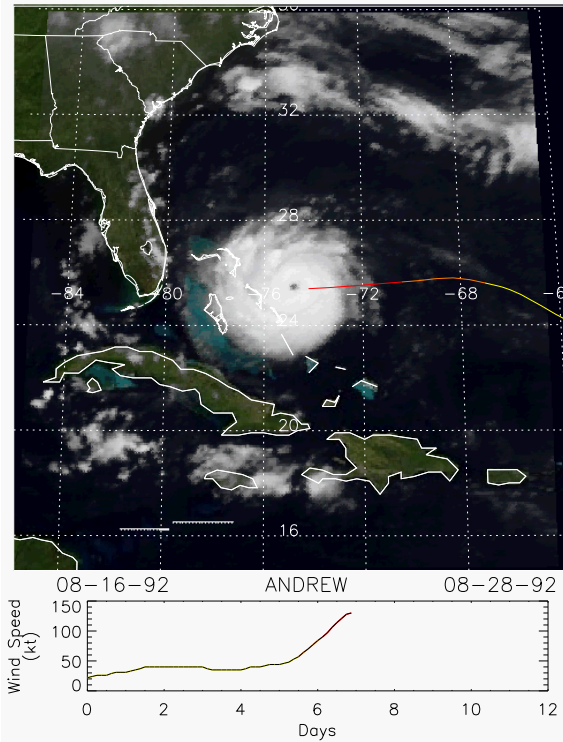
746 Clusters over land and those that formed north of 30° latitude were removed.

747

748

749

750



751

752 Figure 4 - HURSAT image of 1992 Hurricane Andrew from August 23, 1992 along with a time
753 series of its maximum sustained wind (in knots).

754 **MPEG/GIF/SWF**

755 Animation location

756 <ftp://eclipse.ncdc.noaa.gov/pub/hursat/b1/v03/mpg/1992230NA11325-AND.mpg>

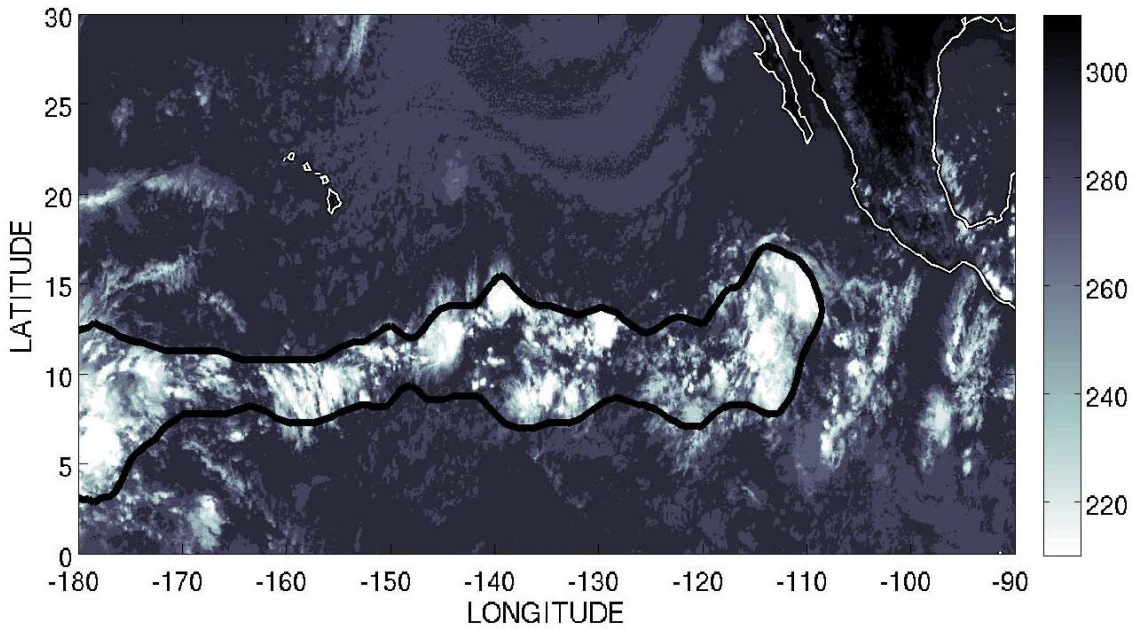
757 (right click link and "Save as..." then open using Windows Media Player, a codec may be
758 required)

759 ftp://eclipse.ncdc.noaa.gov/pub/misc/kknapp/bams_grisat/andrew.gif or

760 ftp://eclipse.ncdc.noaa.gov/pub/misc/kknapp/bams_grisat/andrew.swf

761

762



763

764 Figure 5 - Example of ITCZ detection in the east Pacific using the statistical model for 18
765 August 2000 at 2100 UTC. The grayscale represents IR temperature (K) from GridSat; the black
766 line outlines the identified location of the ITCZ. The North American coastline is outlined in
767 white.

768 **GIF/SWF**

769 Animation location:

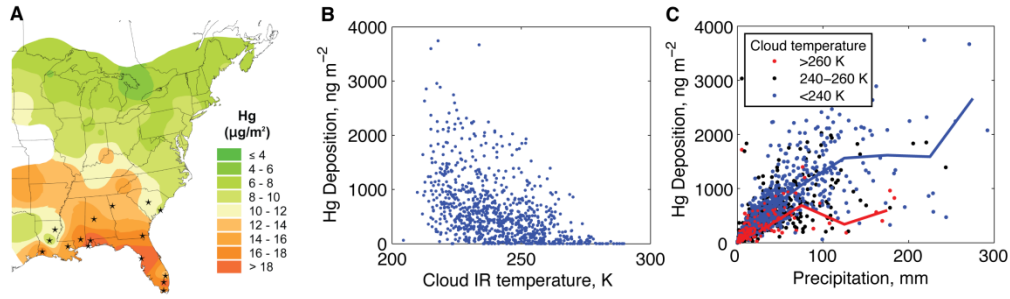
770 ftp://ftp.ncdc.noaa.gov/pub/data/papers/bams_grisat/IRloop.gif or

771 ftp://eclipse.ncdc.noaa.gov/pub/misc/kknapp/bams_grisat/IRloop.gif or

772 ftp://eclipse.ncdc.noaa.gov/pub/misc/kknapp/bams_grisat/IRloop.swf

773

774

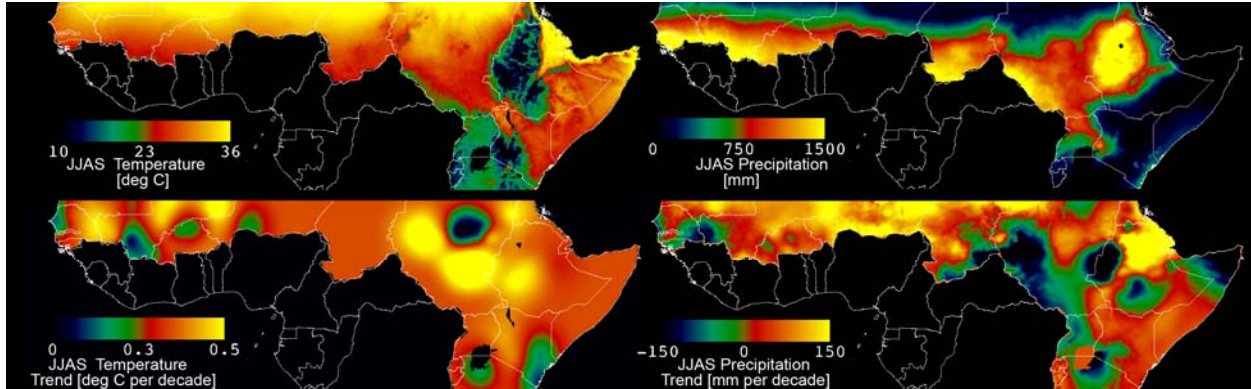


775

776 Figure 6 - (A) Mercury wet deposition in the eastern United States for 2005. Stars show sites
777 analyzed here. (B) Mercury wet deposition for summers 2001-2006 and mean infrared (IR) cloud
778 temperature from GridSat IR. (C) Mercury wet deposition and precipitation for three different
779 cloud temperature ranges. Lines show mean concentration in 50 mm precipitation bins for the
780 coldest (temperature $< 240\text{K}$) and warmest (temperature $> 260\text{K}$) clouds. [Figures adapted from
781 (Holmes 2008; Holmes et al. 2011)(Mercury Deposition Network 2006)]

782

783



784

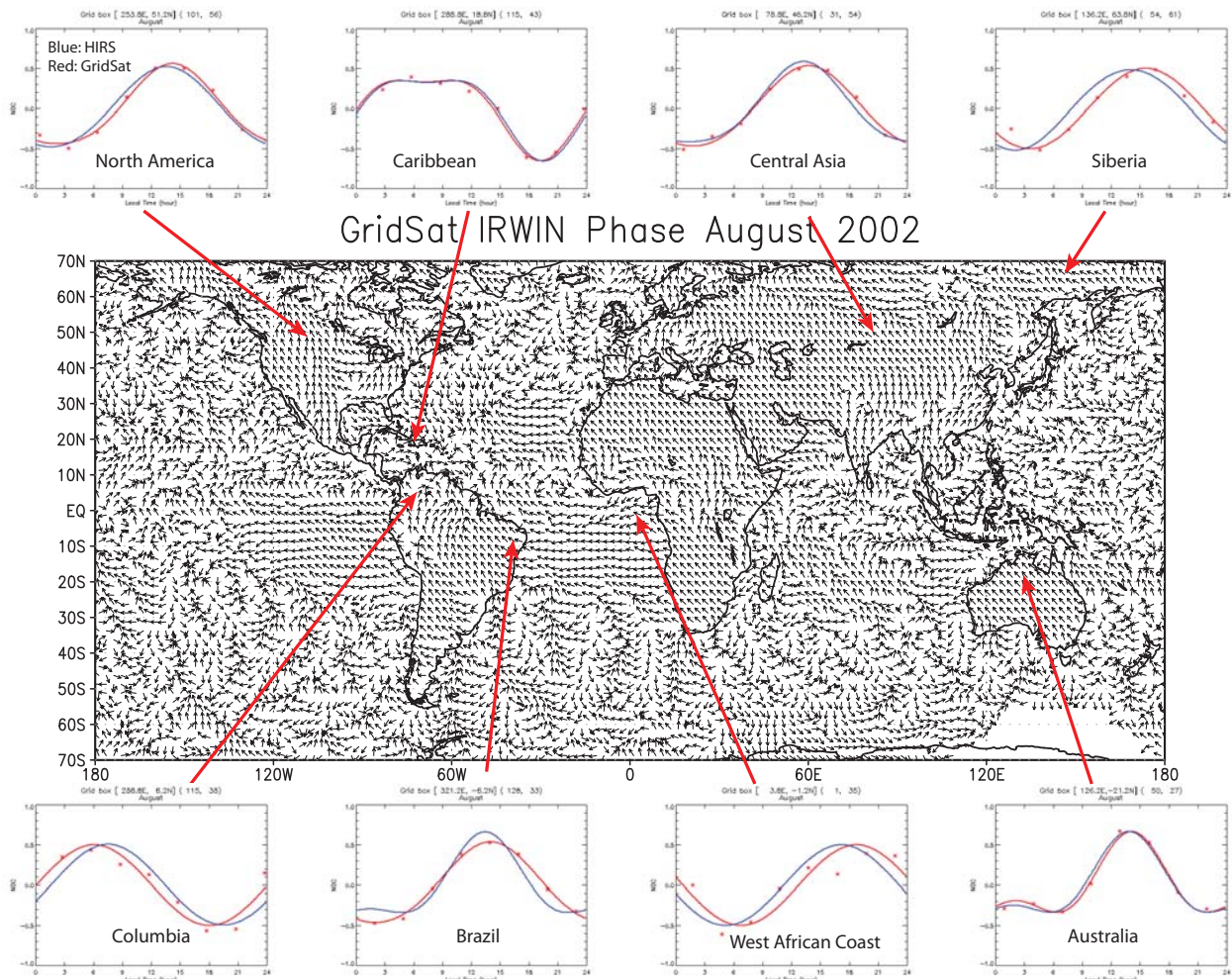
785

786 Figure 7 – June-September (JJAS) air temperature and rainfall estimates based on combinations
787 of GridSat infrared fields and in situ station observations. The top two panels show decadal
788 average air temperature (left) and rainfall (right) for the 1999-2008 period. The bottom panels
789 show the differences between these decadal averages and the 1984-1993 average (the 1999-2008
790 average minus the 1984-1993 average).

791

792

793



794

795 Figure 8 - Comparison of diurnal OLR models from the HIRS climatology and GridSat for
 796 August 2002. The GridSat OLR helps to verify the representativeness of the climatological OLR
 797 diurnal models used in the production of the HIRS OLR climate data record. The arrows in the
 798 central panel indicate the phases of the OLR diurnal models with the 12 o'clock local time
 799 pointing north, running counter-clockwise. The surrounding plots compare the diurnal models
 800 for selected regions with distinctively different types of diurnal variations. The mean values of
 801 GridSat OLR in each diurnal plot were adjusted to those of the HIRS to aid visual comparison.

802

803

804

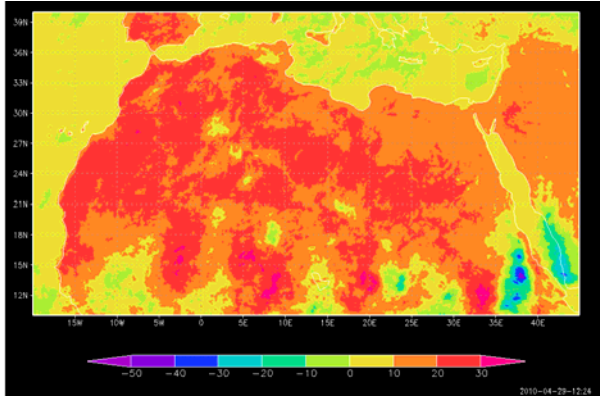
```
#!/bin/bash

for hour in 00 03 06 09 12 15 18 21
do
  ncra GRIDSAT-B1.2002.07.??.$hour.nc \
    -d lat,10.,40. -d lon,-20.,45. -v irwin \
    -o GRIDSAT-B1.2002.07.$hour.nc
done
ncrcat GRIDSAT-B1.2002.07.??.$hour.nc -o GRIDSAT-B1.2002.07.nc
```

805

806 Figure SB1 – BASH code that uses netCDF operators to process one month of GridSat data of
807 the Sahara Desert into diurnally-averaged brightness temperatures.

808



809

810 Figure SB2 – Average daily IR TOA temperature change (K) between 3 UTC and 15 UTC over

811 the Saharan desert for August 2002.